Received: 28 June 2024 | Revised: 29 August 2024 | Accepted: 5 September 2024

DOI: 10.1111/jace.20171

Journal of the American Ceramic Society

RESEARCH ARTICLE

Local structure maturation in high entropy oxide $(Mg,Co,Ni,Cu,Zn)_{1-x}(Cr,Mn)_xO$ thin films

Gabriela E. Niculescu[1] | **Gerald R. Bejger**[1,2] | **John P. Barber**[1,2] | **Joshua T. Wright**[3] | **Saeed S. I. Almishal**[4] | **Matthew Webb**[5] | **Sai Venkata Gayathri Ayyagari**[4] | **Jon-Paul Maria**[4] | **Nasim Alem**[4] | **John T. Heron**[5] | **Christina M. Rost**[1,2]

[1]Department of Physics and Astronomy, James Madison University, Harrisonburg, Virginia, USA

[2]Department of Materials Science and Engineering, Virginia Polytechnic Institute and State University, Blacksburg, Virginia, USA

[3]Department of Physics, Illinois Institute of Technology, Chicago, Illinois, USA

[4]Department of Materials Science and Engineering, The Pennsylvania State University, University Park, Pennsylvania, USA

[5]Department of Materials Science and Engineering, University of Michigan, Ann Arbor, Michigan, USA

Correspondence
Christina M. Rost, Department of Materials Science and Engineering, Virginia Polytechnic Institute and State University, Blacksburg, VA 24061, USA.
Email: cmrost@vt.edu

Funding information
NSF through the Materials Research Science and Engineering Center DMR, Grant/Award Number: 2011839

Abstract

High entropy oxides (HEOs) have garnered much interest due to their available high degree of tunability. Here, we study the local structure of $(MgNiCuCoZn)_{0.167}(MnCr)_{0.083}O$, a composition based on the parent HEO $(MgNiCuCoZn)_{0.2}O$. We synthesized a series of thin films via pulsed laser deposition at incremental oxygen partial pressures. X-ray diffraction shows lattice parameters to decrease with increased pO_2 pressures until the onset of phase separation. X-ray absorption fine structure shows that specific atomic species in the composition dictate the global structure of the material as Cr, Co, and Mn shift to energetically favorable coordination with increasing pressure. Transmission electron microscopy analysis on a lower-pressure sample exhibits a rock salt structure, but the higher-pressure sample reveals reflections reminiscent of the spinel structure. In all, these findings give a more complete picture of how $(MgNiCuCoZn)_{0.167}(MnCr)_{0.083}O$ forms with varying initial conditions and advances fundamental knowledge of cation behavior in high entropy oxides.

KEYWORDS
high entropy oxides (HEOs), pulsed laser deposition (PLD), thin films, X-ray absorption fine structure (XAFS)

1 | INTRODUCTION

The emergence of high entropy oxides (HEOs) in materials science has opened the possibilities of novel ceramics design with a high tunability space. In the simplest definition, HEOs are usually composed of four or five cations present in equimolar or near equimolar amounts that randomly occupy relevant sites over the crystalline sublattice.[1] The seminal HEO was synthesized in 2015 of the structure $(MgZnNiCoCu)_{0.2}O$ and commonly referred to as J14.[2]

Gabriela E. Niculescu, Gerald R. Bejger, and John P. Barber contributed equally to this work.

Since then, HEOs have garnered much attention for their wide range of compositions and potential use in electrical, magnetic, and optical fields, among other applications.[3–10] J14 consists of a single phase, disordered oxide exhibiting the rock salt structure and containing an equal distribution of Mg, Co, Ni, Cu, and Zn on the cation sublattice. The possible compositions, structures, and applications of HEOs and related ceramics are wide-ranging and continue to emerge and expand.[11–18]

The seminal HEO exhibited a rock salt structure, but since then, several other crystal symmetries have been successfully synthesized using a variety of techniques including solid-state method,[2,5] pyrolysis,[19] floating zone,[20] and pulsed laser deposition.[21–24] Spinel[7,8,14,25,26] and perovskite-type structures[5,27,28] have gained much attention in recent years due to their more complex sublattices, which can be utilized for unique property tuning.[29] Initial studies explored well-known arguments, such as the Goldschmidt tolerance factor,[30] to explain the observed stabilities of perovskites. Notably, spinel-based compositions enable cations normally prone to lower-symmetry structures to be incorporated into a higher-order symmetry system. HEO spinels have also been shown to have a smaller band gap than any of the parent oxides in the composition, expanding the repertoire of synergistic effects brought about by the high entropy landscape.[8] Alkali metal-doped HEO compositions were measured to have a large dielectric constant and superior ionic conductivity enabling applications in energy storage.[3,4] High entropy rare-earth oxides (HREOs) added fluorite and bixbyite structures to the list.[31,32] HREOs are marked by a low thermal conductivity and a tunable band gap that can be used in coatings and optics, respectively.[33–35] Other properties currently under investigation show promise that HEOs may also find applications in ferroelectrics and magnetism.[14,28,36–39]

Much prior research has focused on the applications and properties of these HEOs as well as characterizing the crystal structure of the compositions. However, less research has been done regarding local structure trends, which have profound effects on observed properties. For example, the octahedral rotation distortions in perovskite oxides have resulted in the emergence of two-dimensional ferroelectricity.[40] Mathematically, the ideal HEO solid solution would have random occupancy, with each permutation of cation arrangement being energetically equivalent. However, Rost, et al. demonstrated that the Cu^{2+} cation exhibits Jahn-Teller distortions[41] within the J14 structure, using extended X-ray absorption fine structure spectroscopy (EXAFS). These distortions show that different cations behave differently despite the global structure being the same. More recent works exploring local structure have shown varying degrees of disorder among cations.[7,13,14,42] Fundamentally, this means that while a system may be high entropy, other factors such as enthalpy cannot be ignored,[43,44] which is a complex and ongoing discussion amongst the community.

In this work, we investigate the cation valence and local structure behavior of select representative atomic species in a series of high entropy oxide thin films grown using pulsed laser deposition under varying pO_2 to advance the fundamental understanding of such materials behavior from a local perspective. In doing so, we also test the efficacy of typical analysis methods of X-ray absorption near-edge fine structure (XANES) commonly used as applied to HEOs. Further, by understanding the underlying behaviors that govern synthesis, we can refine future synthesis pathways of HEOs with more precise tunability.

2 | METHODS

Composition $(MgNiCuCoZn)_{0.167}(MnCr)_{0.083}O$ (J14CrMn) was synthesized for this study based on the “standard” J14 parent HEO.[2] The powders were mixed using the following binary oxide components: MgO (Sigma Aldrich, 342793, 99% trace metals basis, -325 mesh), NiO (Sigma Aldrich, 399523, -325 mesh, 99%), CuO (Sigma Aldrich, 450812, 99.99% trace metal basis), CoO (Sigma Aldrich, 343153, -325 mesh), ZnO (Sigma Aldrich, 255750, 99.99% trace metal basis), Mn_3O_4 (Sigma Aldrich, 377473, 97%), and Cr_2O_3 (Alfa Aesar, 12285, 99% trace metals). The powders were massed accordingly for the desired stoichiometry, listed in Table S1, and mixed/milled using a Spex 8000 M Mixer Mill using three 5 mm yttrium-stabilized zirconia milling media for 1 h.

After mixing, the powder was uniaxially pressed into a 25 mm pellet at 5500 pounds per square inch (psi) for 30 s (Carver Platen 2). The pellet was sintered in air at 1000°C for 8 h with a ramp rate of 4°C/min using a SentroTech STT-1700°C tube furnace and air quenched. The resulting phases of the reactively sintered target were identified using X-ray diffraction and are shown in Figure S1.

$(MgCoNiCuZn)_{0.167}(CrMn)_{0.0835}O$ films were deposited on (001)-oriented MgO substrates by ablation from a 248 nm KrF laser fired at 5 Hz and 1.7 J cm^{-2} with a spot size of ~ 0.05 cm^2 for a total of 10000 pulses. The substrates were pre-annealed at 950°C in a base vacuum for 20 mins prior to being held at 400°C in a pressure series (1, 2, 3, 4, 5, 7.5, 10, 15, 25, and 50 mTorr) of pure O_2 throughout the deposition before cooling at the same pressure. The substrate-target distance was 7 cm.

X-ray diffraction (XRD) was performed on the reactively sintered targets for phase identification using a PANalytical X’Pert Pro MPD. Measurements were taken using a theta-theta goniometer equipped with diverging beam optics and an X'celerator detector. Scans ranged from 15° to 80° 2θ with a step size of 0.033°/step and dwell time of 200 s/step. Phase identification was performed using Highscore Plus.[45] Films were measured in 2θ-ω with a Rigaku Smartlab diffractometer, using a 1.54 Å Cu Kα source, a Ge 220 monochromator, and parallel beam geometry. A 5 mm slit was used, with a 0.1° step size; for narrow scans, the speed was 1°/min, while for broad scans the speed was 12°/min.

Transmission electron microscopy (TEM) sample preparation was performed using the Thermo Fisher Helios 660 NanoLab Dual-Beam FIB. The FIB lamellae were thinned down with a 5 kV ion beam, and final cleaning was carried out with 2 and 1 kV ion beams to reduce Ga^+ ion damage. The Thermo Fisher Talos F200 × 2 was used to obtain selected area electron diffraction (SAED) patterns at 200 kV.

X-ray absorption fine structure spectroscopy (XAFS) was performed on beamline 10-BM[46] at the Advanced Photon Source, Argonne National Laboratory (Lemont, IL). The films were suspended in a nylon washer and wrapped in Kapton tape to be measured in fluorescence yield using a Si (111) monochromator, detuned 50% for harmonic rejection, and a Hitachi 4-element Vortex ME-4 SDD (Tokyo, Japan) detector. The beamline was calibrated using a standard set of metal foils. In addition, these foils remained in the beam for transmission measurements allowing scan-by-scan energy alignment and ensuring energy calibration for each sample. The K-edges for cobalt (7709 eV), manganese (6539 eV), and chromium (5989 eV) were targeted for this study due to their well-known variability in valence states, and each sample was scanned on every absorption edge between 3 and 5 times. The samples were scanned up to $k = 13$ Å^{-1}. Data was processed and analyzed using the Demeter software package.[47]

Analysis of the XANES data consisted of extracting information on valence state and coordination through comparison to spectral reference standards from literature.[50,53,54] The literature standards were compared to the respective metal foils measured with our samples to ensure a correct energy grid alignment. Arcon, et al. demonstrated that the energy shift of the Cr K-edge is linearly proportional to the valence state for materials systems containing the same ligand type.[48] By similar methods, estimation of the Co, Mn, and Cr valence states in J14CrMn was performed. The energy shift, ΔE_0, was calculated by subtracting the metal edge energy from the edge energy for each sample. The edge energy, E_0, can be defined in several ways including using white line maxima or peaks in the first derivative of the edge region. If consistency is maintained throughout each absorber, the relative shift between edge energies can be used to estimate average valence. E_0 for Cr and Co absorbers was chosen to be the middle peak in the first derivative, excluding the pre-edge, while the Mn E_0 was chosen to be the last peak in the first derivative due to noise. Coordination information is extracted by fingerprinting the features of the spectra standards to the collected data.

3 | RESULTS AND DISCUSSION

XRD of the reactively sintered target contains three crystallographic phases including rocksalt, spinel, and tenorite, shown in Figure S1. Due to the similar scattering cross sections[49] of the constituent elements, we are unable to discern the exact composition of each particular phase. Using PLD for film growth enables target stoichiometry to be controlled in the synthesis of single-phase epitaxial structures.[22,25,50,51] Approximately 90 nm thick films grown epitaxially along the [001] direction at constant temperature on [100] MgO substrates with increasing pO_2 from 1 to 50 mTorr, shown in Figure S2. Crystallization appears at 2 mTorr pO_2. In the lower pressure regime, between 2 and 10 mTorr, the (002) film peak further crystalizes as evidenced by the formation of Pendellösung fringing, then begins to shift toward a smaller out-of-plane lattice parameter at 5 mTorr. Above 10 mTorr, the film peak appears to suggest strain, as evidenced by the asymmetry of the film peak and ultimately what may be the onset of phase separation. Full-range scans from 30 to 100 °2θ shown in Figure S3 confirm epitaxial growth with no additional peaks present. Further, images of 5, 10, and 50 mTorr pO_2 film surfaces using scanning electron microscopy (SEM) are shown in Figure S4.

The analysis of the XANES region can be used to provide information such as valence state, coordination number, and differences in the local environment.[52] A comparison of measured XANES to known literature references[48,53,54] is shown in Figure 1. Changes in key fine structure features, denoted by arrows, show the local stereochemical evolution of absorbing cations. The pre-edge features in first-row transition metals correspond to the 1s → 3d transition[55] and provide insight into coordination numbers. Initially, as prepared under the lower pO_2, we see a primarily Cr^{3+}-dominated environment shown in shown in Figure 1A. This is observed in the XANES data by broad, pre-edge shoulder matching literature references for Cr^{3+} in an octahedral environment.[48] As pO_2 is increased in subsequent depositions there is a systematic change in the Cr coordination indicative of 4-coordinated polyhedra,[56] where a sharp pre-edge feature near 5992 eV develops and eventually comes to dominate the pre-edge structure. Further, the white line peak at ~6007 eV takes on a single peak instead of the double peak we see in the 3^+ state, and the region just above the edge (~6030 eV) increases

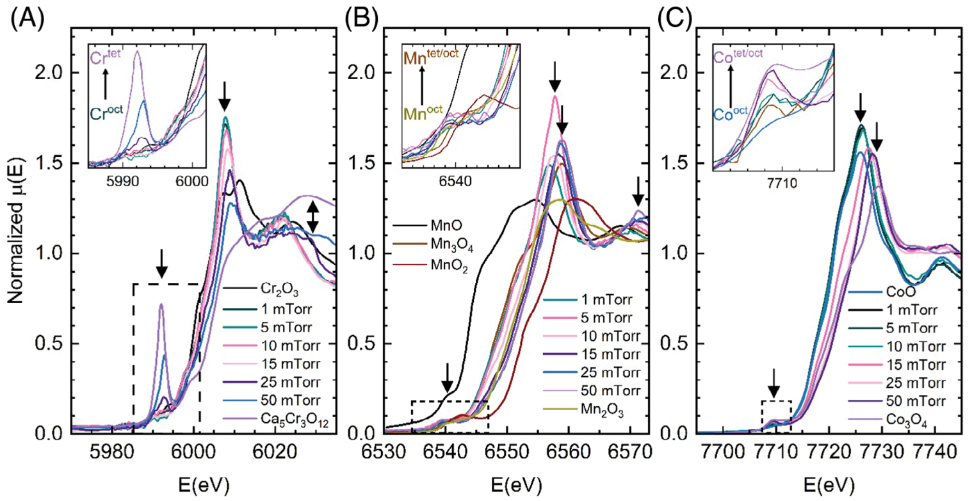

FIGURE 1 X-ray near edge structure (XANES) of select absorbers (A) Cr, (B) Mn, and (C) Co. Arrows indicate main features in spectra. The inset for each panel shows the pre-edge feature comparison between samples and literature references discussed in the main text. The Y-axis label in panel (A) applies to all panels in the figure.

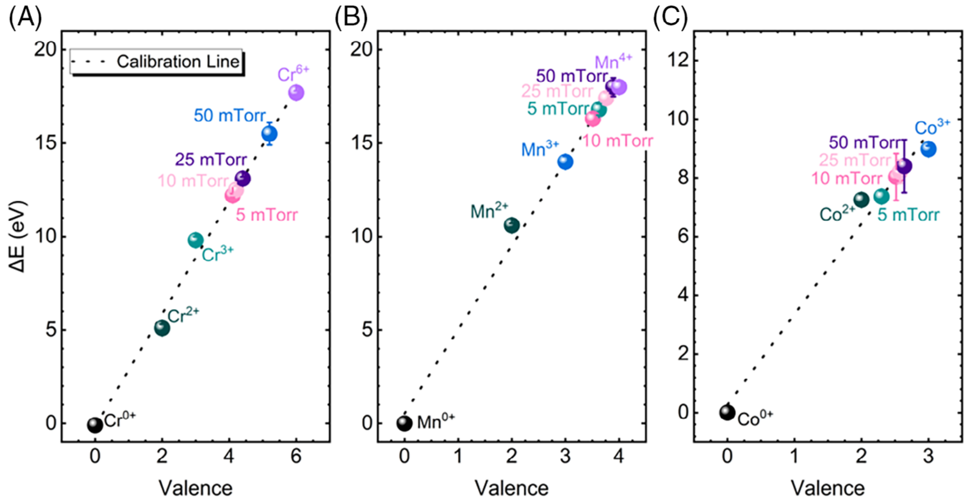

FIGURE 2 Plot of ΔE versus cation valence for (A) Cr, (B) Mn, and (C) Co. Y-axis label and units in panel (A) apply to all panels in the figure.

in intensity toward that of the 6^+ reference. Mn, shown in Figure 1B, increases in average valence between 3^+ and 4^+ with increasing pO_2 as indicated by the energy shift of the K-edge. The pre-edge features denoted by the arrow at ~6540 eV appear consistently throughout the pressure series and are consistent with octahedral coordination. For Co, in Figure 1C, the spectra shift more toward the Co^{3+} standard as pressure increases. The pre-edge feature also begins to increase intensity indicating a transition from octahedral toward a mixed occupation of octahedral/tetrahedral environment.

Using the strategy of Alcorn, et al.[48] mentioned previously, the relative change of the $\Delta E_{0,}$ or the edge energy shift, versus the valence is plotted in Figure 2. The valence state can be estimated by the energy shift of the absorption edge relative to a known standard, typically a pure metal. The ΔE_0 of the 5, 10, 25, and 50 mTorr samples were compared to standards and used to estimate valence in all three absorbers. Linear regression analysis of the ΔE_0 versus valence of known standards provided a calibration line. Inserting the measured ΔE values for each sample into the corresponding linear equation enables one to determine the total average valence of the absorbing species. In Figure 2A, Cr appears to transition from an average of 4^+ at 5 mTorr toward 5.5^+ at 50 mTorr $pO_{2.}$ Mn (Figure 2B) has an average valence trending from ~3.5^+ to 4^+. Finally,

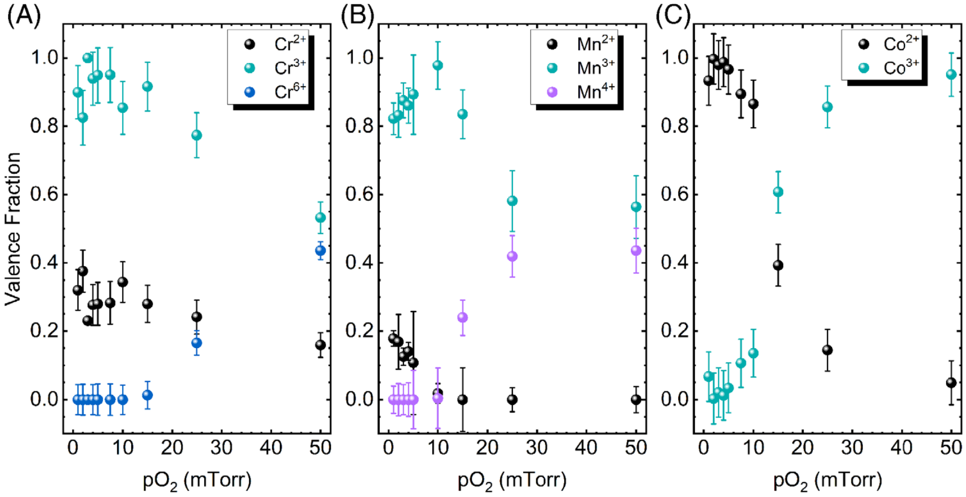

FIGURE 3 Plot of valence fraction versus pO_2 achieved by linear combination fitting (LCF). The Y-axis label in panel (A) applies to all panels in the figure. An example of fitting is in Figure S5.

Co has an average valence of ~2.3 and ~2.6 at 5 mTorr and 50 mTorr pO_2, respectively, as shown in Figure 2C.

Linear combination fitting (LCF) was performed to support the valence trend results across Co, Cr, and Mn absorbers, respectively, as shown in Figure 3A–C. The Cr absorber data begins at low pressures with a mixed valence heavily weighted toward 3^+. Above 15 mTorr, the fraction of 3^+ begins to decrease, with an appearance of 6^+ beginning at 25 mTorr. At 50 mTorr, there is a mixed valence of 3^+ and 6^+ with fractions of 0.53 and 0.43, respectively, the remaining fraction being most likely held by 2^+. The Mn absorber starts fully in the 3^+ valence state for lower pressures, with the 4^+ valence state emerging above 7.5 mTorr deposition pressure. At 15 mTorr, 4^+ overtakes 3^+ as the predominant state with fractions of 0.57–0.43. The fraction of 4^+ increases to ~0.7 at the 25 and 50 mTorr data points. Finally, the Co absorber has a valence of 2^+ from 1 to 10 mTorr pO_2, a mixed-valence with a majority of 2^+ at 15 mTorr, and then mixed with a majority of 3^+ at higher pO_2.

It is important to note the limitations of conventional LCF, especially within the context of HEOs containing several transition metal elements. The challenge is 2-fold: finding a literature or measurable standard to use as a component and accounting for relative changes in feature intensity (like white lines) due to sample geometry and beam polarization effects. Here, we used LCF to ascertain valence trends in Cr, Mn, and Co absorbers by fitting a weighted sum of standards found in the literature based on the valence state. It is nearly impossible to account for all deviations in white line intensities or pre-edge features given that not all permutations of valence, geometry, and coordination have specific reference standards or known crystal systems. The takeaway of our multifaceted XANES analysis is that the trends are consistent and generally in agreement, thus strengthening confidence in our findings.

Figure 4 illustrates the magnitude and imaginary parts of the Fourier-transformed k2-weighted EXAFS for a number of cases where we see a clear and observable trend within the first coordination shell. To investigate the first coordination shell, we fitted the spectra using a theoretical model with a single scattering path between the absorber and nearest neighbor oxygens. At low pressures, the film appears to be amorphous per XRD results, shown in Figure S2. EXAFS, however, does not depend on long-range order in the system. Therefore, to understand the synthesis trends from a local perspective we choose the 1 mTorr sample as a baseline for the first shell environment. For some atoms, like Mn where the coordination number reaches a steady state with increasing pressure, we can extrapolate radial distances and unit cell parameters. These results match the bond lengths and unit cell parameters found via XRD for the samples, thus giving a reasonable basis for studying the metal-oxygen bond. The second shell corresponds to the metal-metal scattering paths, which remain largely stable. Modeling of this length, however, is limited by the stoichiometric ratios and the effects of various scatterers similar in mass at similar distances. The range from $k = 6–8$ Å^{-1} demonstrates a poor fit for first shell scatterers. This is because this range is largely indicative of the heavier scatterers in the sample. A linear combination of both fit sets yields an approximate solution for the full structure. Note that although a solution exists, the uncertainties arising from the unknown mass of the metal-metal scatterer restrict the amount of information that can be confidently drawn. Therefore, it is better used as a guide rather than an exact fit.

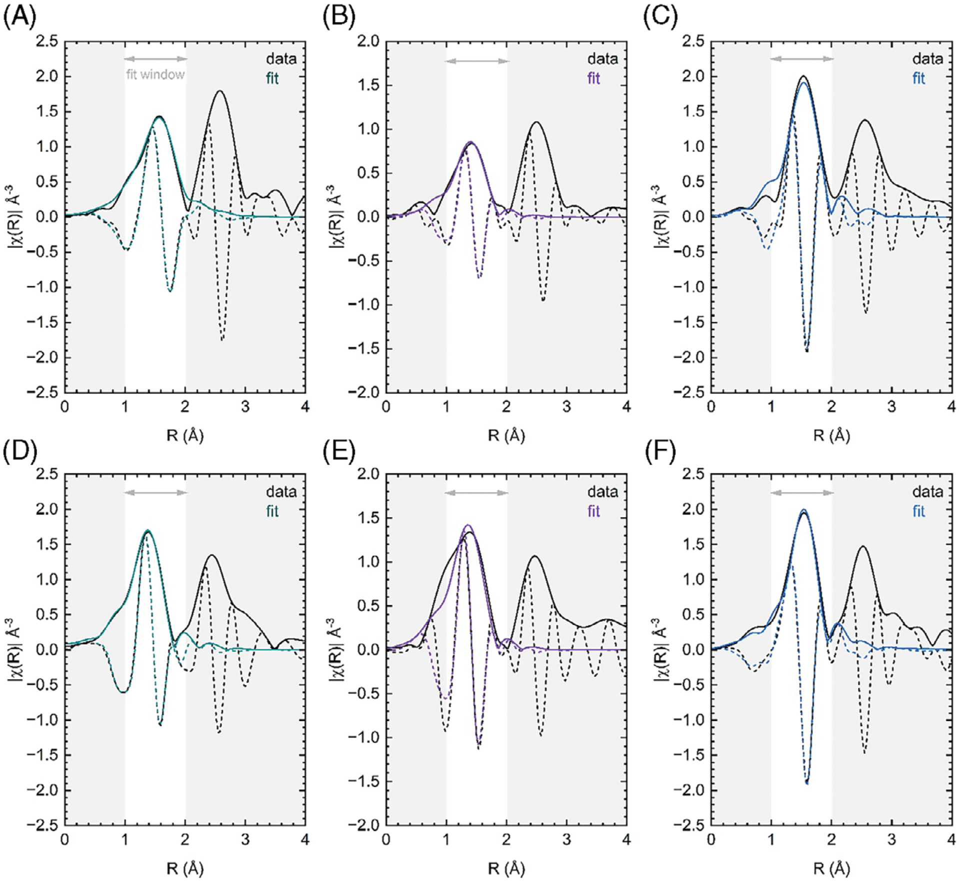

FIGURE 4 Magnitude and imaginary parts of the Fourier transformed k^2-weighted extended X-ray absorption fine structure spectroscopy (EXAFS) for (A) Co at 3 mTorr O_2, (B) Mn at 1 mTorr O_2, (C) Cr at 2 mTorr O_2, (D) Co at 25 mTorr O_2, (E) Mn at 15 mTorr O_2, and (F) Cr at 15 mTorr O_2.

Figure 5 plots the average coordination number as a function of pO_2 for Co, Cr, and Mn. The results for Mn display a relatively stable coordination environment, within uncertainty, in the pO_2 range corresponding to the highest crystallinity. While there are minor fluctuations, likely due to the noise of the Mn spectra, the short range of the fit restricts the number of independent variables. Our conclusions are drawn from the first shell fits for each absorber element. Accurate modeling of the metal-metal distance would require a variable set of metals with closely similar atomic masses. We trade the information and resolution of the results for more clarity on the well-known bonding between metal and oxygen. Therefore, when we consider the results shown in Table S2. For Mn, the coordination number is $4.5^{\pm}$ ~0.5. This indicates a nearly 50/50 mix of Mn in both the 4-fold and 6-fold coordinated states at 10mTorr. For Cr, the coordination environment undergoes an onset phase-transition-like process where the coordination number starts at 6 but then converts to 4-fold symmetry after about 15 mTorr of pO_2 is introduced. We theorize that once there is sufficient oxygen for cations to undergo a change of valence, and subsequent change in ionic radius, a more energetically favorable polyhedral state, based on close packing, is formed around certain cations that become incorporated into the larger structure. We propose that in-plane bonding remains strong; this is the 4 coordinated, tetragonal state environment we see dominating at higher pO_2. The out-of-plane bonding, however, exhibits compression and expansion based on the partial pressure of O_2. A handful of atoms, like Mn and Cu, hold the larger superstructure together, as demonstrated by the unchanged mixed-fold coordination we would expect. This suggests that a spinel might be forming as the bonds are strained with the increased oxygen sites and decreased valence electrons available to form bonds.

SAED experiments using TEM were carried out to investigate the structural nuances in the thin films grown at 5 mTorr and 50 mTorr O_2. From the TEM diffraction patterns shown in Figure 6, we observed a clear variation in the crystal structure of the thin films grown at different O_2 partial pressures from the selected area electron diffraction experiment. J14CrMn grown at 5 mTorr indicates a rock salt crystal structure, while J14CrMn grown

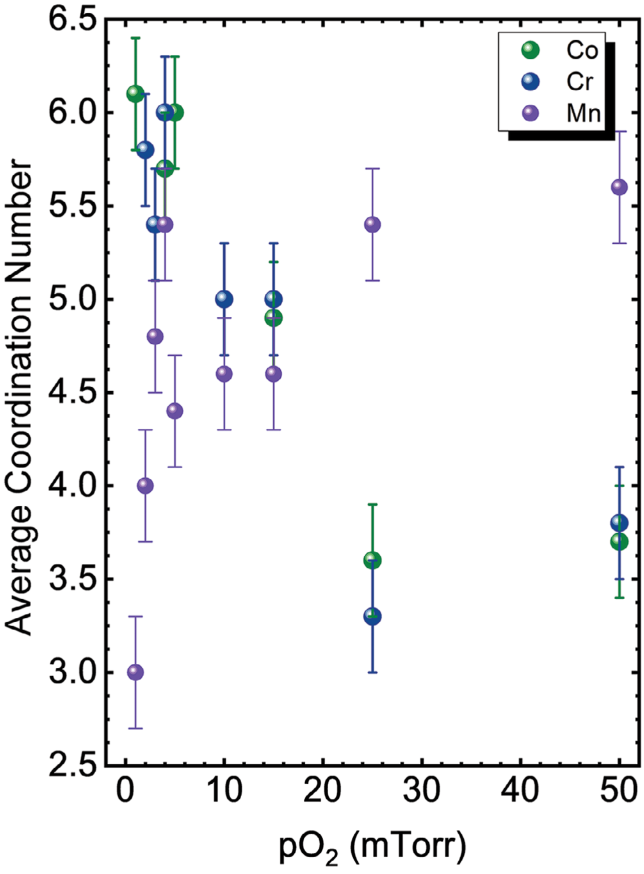

FIGURE 5 Coordination number versus oxygen partial pressure for Co, Cr, and Mn absorbers.

at 25 mTorr and 50 mTorr has a rock salt structure with additional reflections (marked by green boxes in Figure 6). To further understand the origin of the extra reflections, selected area electron diffraction was performed along the [110] zone axis for the 50 mTorr sample (shown in Figure S6). These extra reflections indicate local structural variations that are consistent with the spinel secondary phase observed in XRD. This is also associated with the changes in the valence state of cations shown in Figure 2. Further, TEM studies are being carried out to probe the local variation in valence states.

Nonequilibrium kinetics by pulsed laser deposition (PLD) is uniquely suited to enable cation's charge state control in high entropy oxides. This is achieved through the metastabilization of unique macrostates at substrate temperatures lower than the entropy stabilization temperature which provides a rich landscape of local structures and valence states.[25,23,57,58] For instance, Kotsonis et al. noted a sharp change in the out-of-plane lattice parameter of J14 thin films with substrate temperature. Electron energy loss spectroscopy (EELS) as well as X-ray absorption spectroscopy (XAS) were employed to inspect the valence state of the core elements in the thin films.[23] Local analysis reveals that at relatively low substrate temperatures, a significant Co 3^+ concentration is present and is attributed to cation vacancies.

We believe that the high configurational entropy and metastability inherent to HEOs facilitate hosting more accepting local environments coupled with unusual coordination and defect chemistry. As such, the degree of tunability and range of lattice parameters and volume changes should increase with compositional complexity. To highlight this, Figure 7 shows two sets of films of $Mg_{0.83}Cr_{0.17}O$ grown 5 and 50 mTorr pO_2 at temperatures of 300 and 500°C, respectively. While the films display a decrease in the out-of-plane lattice parameter with increasing deposition pressure, the degree of the shift is less pronounced than in the high entropy case. Therefore, we need specialized characterization techniques to understand the local structures and cation valence in high configurational entropy systems and how they deviate from their lower entropy counterparts.

By examining the behavior of local structure as a function of deposition pressure, we can better understand the long-range behavior of these materials. Combining the information from XANES and EXAFS gives us a more complete picture of how individual atomic species respond to the evolving structure as deposition pressure varies. While the transition between valence states can be modeled with a power law, it is important to consider that it may not be possible to tune with a great deal of resolution. The onset occurs over a very short range of partial pressures. Maintaining specific levels during deposition is an ongoing area of study to control these tunable aspects. Notably, a localized expansion was found around the Mn atom. This indicates that not all atoms are equally affected in their transition. These differences could be ascribed to the relative masses of other cations. Soft X-ray sources might yield information about the oxygen environment; however, due to the expanse of bonding options deconvoluting the oxygen, XANES is speculative at best.

One of the motivations driving the development and study of HEOs is their potential properties. The seminal structure HEO J14 is found to have a long-range antiferromagnetic ground state with unique spin-state interactions.[59] Testing the magnetic properties as a function of the deposition pressure of J14CrMn may allow us to further understand the effects of local structure on global properties. Future research could delve into the changes in magnetic structure associated with different valence states. Furthermore, if experimental findings could be corroborated with theoretical calculations, then this allows us to finely tune the structure and deposition conditions for HEOs.

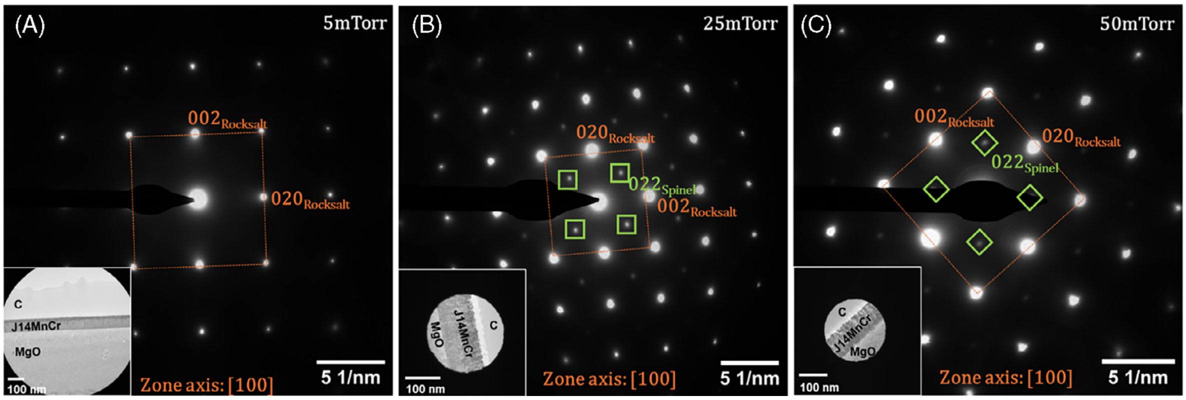

FIGURE 6 Selected area electron diffraction of J14MnCr at (A) 5 mTorr O_2, (B) 25 mTorr O_2, and (C) 50 mTorr O_2. Green boxes in (B) and (C) highlight the presence of extra reflections that are typically absent in a perfect rock salt structure.

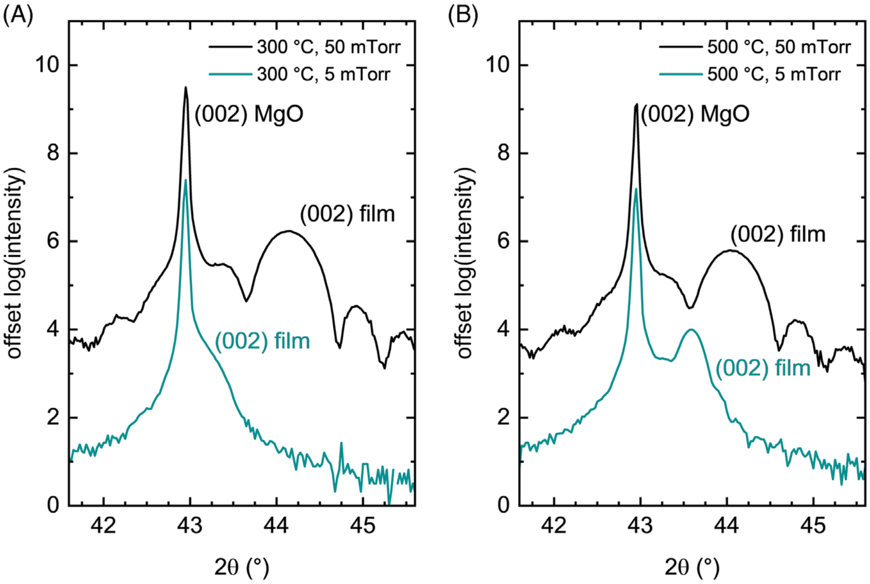

FIGURE 7 X-ray diffraction (XRD) of two $Mg_{0.83}Cr_{0.17}O$ films grown at (A) 300°C, 5 and 50 mTorr pO_2 and (B) 500°C, 5 and 50 mTorr pO_2 at a constant 1.2 J/cm^2 fluence.

4 | CONCLUSION

Seven-component HEO $(MgNiCuCoZn)_{0.167}(MnCr)_{0.083}O$ (J14CrMn) was successfully synthesized using pulsed laser deposition with varying initial conditions. This study examined the local structure of this material to gain a deeper understanding of how this emerging class of materials behaves. For J14CrMn, the lattice parameter decreases as partial oxygen pressure increases, which is the opposite trend of the seminal J14 structure. According to XANES analysis, the valence state and coordination number are also dependent on the partial pressure of oxygen, with a phase shift occurring as pressure is increased in the Cr, Mn, and Co absorbers. A close study of the metal-oxygen paths via EXAFS supports the XANES data, as Cr shifts from 6-fold to energetically favorable 4-fold when sufficient oxygen is introduced to the system. These changes in coordination suggest a spinel phase formation as a result of bond strains introduced by fewer valence sites. Finally, SAED results indicate the spinel structure forming as deposition pressure is increased, thus supporting both the XRD and EXAFS analysis. From these results, we theorize that while in-plane bonding is stable, it is the out-of-plane bond lengths that change with pressure. We observe a select few atoms remaining consistent and dictate the larger superstructure, while other atoms shift in coordination.

ACKNOWLEDGMENTS

The authors acknowledge the support from NSF through the Materials Research Science and Engineering Center DMR 2011839. Sector 10 MRCAT operations are supported by the Department of Energy and the MRCAT member institutions. This research used resources from the Advanced Photon Source, a US Department of Energy

(DOE) Office of Science User Facility operated for the DOE Office of Science by Argonne National Laboratory under Contract No. DE-AC02-06CH11357.

CONFLICT OF INTEREST STATEMENT

The authors declare no conflict of interest.

ORCID

John P. Barber https://orcid.org/0000-0001-9244-5725
Saeed S. I. Almishal https://orcid.org/0000-0003-2964-6000
Jon-Paul Maria https://orcid.org/0000-0003-3604-4761
Christina M. Rost https://orcid.org/0000-0002-6153-6066

REFERENCES

1. Brahlek M, Gazda M, Keppens V, Mazza AR, Mccormack SJ, Mielewczyk-Gryń A, et al. What is in a name: defining "high entropy" oxides. APL Mater. 2022;10:110902.
2. Rost CM, Sachet E, Borman T, Moballegh A, Dickey EC, Hou D, et al. Entropy-stabilized oxides. Nat Commun. 2015;6:8485.
3. Bérardan D, Franger S, Meena AK, Dragoe N. Room temperature lithium superionic conductivity in high entropy oxides. J Mater Chem A. 2016;4:9536–41.
4. Bérardan D, Franger S, Dragoe D, Meena AK, Dragoe N. Colossal dielectric constant in high entropy oxides. Phys Status Solidi RRL—Rapid Res Lett. 2016;10:328–33.
5. Zhou S, Pu Y, Zhang Q, Shi R, Guo Xu, Wang W, et al. Microstructure and dielectric properties of high entropy $Ba(Zr_{0.2}Ti_{0.2}Sn_{0.2}Hf_{0.2}Me_{0.2})O_3$ perovskite oxides. Ceram Int. 2020;46:7430–37.
6. Witte R, Sarkar A, Kruk R, Eggert B, Brand RA, Wende H, et al. High-entropy oxides: an emerging prospect for magnetic rare-earth transition metal perovskites. Phys Rev Mater. 2019;3:034406.
7. Johnstone GHJ, González-Rivas MU, Taddei KM, Sutarto R, Sawatzky GA, Green RJ, et al. Entropy engineering and tunable magnetic order in the spinel high-entropy oxide. J Am Chem Soc. 2022;144:20590–600.
8. Katzbaer RR, Dos Santos Vieira FM, Dabo I, Mao Z, Schaak RE. Band gap narrowing in a high-entropy spinel oxide semiconductor for enhanced oxygen evolution catalysis. J Am Chem Soc. 2023;145:6753–61.
9. Braun JL, Rost CM, Lim M, Giri A, Olson DH, Kotsonis GN, et al. Charge-induced disorder controls the thermal conductivity of entropy-stabilized oxides. Adv Mater. 2018;30:1805004.
10. Sarkar A, Wang Q, Schiele A, Chellali MR, Bhattacharya SS, Wang D, et al. High-entropy oxides: fundamental aspects and electrochemical properties. Adv Mater. 2019;31:1806236.
11. Musicó BL, Gilbert D, Ward TZ, Page K, George E, Yan J, et al. The emergent field of high entropy oxides: design, prospects, challenges, and opportunities for tailoring material properties. APL Mater. 2020;8:040912.
12. Tomboc GM, Zhang X, Choi S, Kim D, Lee LYS, Lee K. Stabilization, characterization, and electrochemical applications of high-entropy oxides: critical assessment of crystal phase–properties relationship. Adv Funct Mater. 2022;32:2205142.
13. Jiang B, Bridges CA, Unocic RR, Pitike KC, Cooper VR, Zhang Y, et al. Probing the local site disorder and distortion in pyrochlore high-entropy oxides. J Am Chem Soc. 2021;143:4193–204.
14. Krysko E, Min L, Wang Yu, Zhang Na, Barber JP, Niculescu GE, et al. Studies on the structure and the magnetic properties of high-entropy spinel oxide $(MgMnFeCoNi)Al_2O_4$. APL Mater. 2023;11:101123.
15. Liu Z-Y, Liu Y, Xu Y, Zhang H, Shao Z, Wang Z, et al. Novel high-entropy oxides for energy storage and conversion: from fundamentals to practical applications. Green Energy Environ. 2023;8:1341–57.
16. Min L, Sretenovic M, Heitmann TW, Valentine TW, Zu R, Gopalan V, et al. A topological kagome magnet in high entropy form. Commun Phys. 2022;5:1–7.
17. Gild J, Zhang Y, Harrington T, Jiang S, Hu T, Quinn MC, et al. High-entropy metal diborides: a new class of high-entropy materials and a new type of ultrahigh temperature ceramics. Sci Rep. 2016;6:37946.
18. Harrington TJ, Gild J, Sarker P, Toher C, Rost CM, Dippo OF, et al. Phase stability and mechanical properties of novel high entropy transition metal carbides. Acta Mater. 2019;166:271–80.
19. Phakatkar AH, Saray MT, Rasul MdG, Sorokina LV, Ritter TG, Shokuhfar T, et al. Ultrafast synthesis of high entropy oxide nanoparticles by flame spray pyrolysis. Langmuir. 2021;37:9059–68.
20. Pressley LA, Torrejon A, Phelan WA, McQueen TM. Discovery and single crystal growth of high entropy pyrochlores. Inorg Chem. 2020;59:17251–58.
21. Mazza AR, Gao X, Rossi DJ, Musico BL, Valentine TW, Kennedy Z, et al. Searching for superconductivity in high entropy oxide Ruddlesden–Popper cuprate films. J Vac Sci Technol A. 2021;40:013404.
22. Kotsonis GN, Rost CM, Harris DT, Maria J-P. Epitaxial entropy-stabilized oxides: growth of chemically diverse phases via kinetic bombardment. MRS Commun. 2018;8:1371–77.
23. Kotsonis GN, Meisenheimer PB, Miao L, Roth J, Wang B, Shafer P, et al. Property and cation valence engineering in entropy-stabilized oxide thin films. Phys Rev Mater. 2020;4:100401.
24. Meisenheimer PB, Kratofil TJ, Heron JT. Giant enhancement of exchange coupling in entropy-stabilized oxide heterostructures. Sci Rep. 2017;7:13344.
25. Rost CM. Entropy-stabilized oxides: explorations of a novel class of multicomponent materials. Raleigh, NC: North Carolina State University; 2016.
26. Dąbrowa J, Stygar M, Mikuła A, Knapik A, Mroczka K, Tejchman W, et al. Synthesis and microstructure of the $(Co,Cr,Fe,Mn,Ni)_3O_4$ high entropy oxide characterized by spinel structure. Mater Lett. 2018;216:32–36.
27. Jiang S, Hu T, Gild J, Zhou N, Nie J, Qin M, et al. A new class of high-entropy perovskite oxides. Scr Mater. 2018;142:116–20.
28. Liu Z, Xu S, Li T, Xie B, Guo K, Lu J. Microstructure and ferroelectric properties of high-entropy perovskite oxides with A-site disorder. Ceram Int. 2021;47:33039–46.
29. Kotsonis GN, Almishal SSI, dos Santos Vieira FM, Crespi VH, Dabo I, Rost CM, et al. High-entropy oxides: harnessing crystalline disorder for emergent functionality. J Am Ceram Soc. 2023;106:5587–5611.

30. Goldschmidt VM. Die Gesetze der Krystallochemie. Naturwissenschaften. 1926;14:477–85.
31. Xu H, Zhang Z, Liu J, Do-Thanh C-L, Chen H, Xu S, et al. Entropy-stabilized single-atom Pd catalysts via high-entropy fluorite oxide supports. Nat Commun. 2020;11:3908.
32. Gild J, Samiee M, Braun JL, Harrington T, Vega H, Hopkins PE, et al. High-entropy fluorite oxides. J Eur Ceram Soc. 2018;38:3578–84.
33. Zheng Y, Zou M, Zhang W, Yi D, Lan J, Nan C-W, et al. Electrical and thermal transport behaviours of high-entropy perovskite thermoelectric oxides. J Adv Ceram. 2021;10:377–84.
34. Lou Z, Zhang P, Zhu J, Gong L, Xu J, Chen Q, et al. A novel high-entropy perovskite ceramics $Sr_{0.9}La_{0.1}(Zr_{0.25}Sn_{0.25}Ti_{0.25}Hf_{0.25})O_3$ with low thermal conductivity and high Seebeck coefficient. J Eur Ceram Soc. 2022;42:3480–88.
35. Sarkar A, Loho C, Velasco L, Thomas T, Bhattacharya SS, Hahn H, et al. Multicomponent equiatomic rare earth oxides with a narrow band gap and associated praseodymium multivalency. Dalton Trans. 2017;46:12167–76.
36. Son Y, Zhu W, Trolier-Mckinstry SE. Electrocaloric effect of perovskite high entropy oxide films. Adv Electron Mater. 2022;8:2200352.
37. Sharma Y, Lee M-C, Pitike KC, Mishra KK, Zheng Q, Gao X, et al. High entropy oxide relaxor ferroelectrics. ACS Appl Mater Interfaces. 2022;14:11962–70.
38. Usharani NJ, Bhandarkar A, Subramanian S, Bhattacharya SS. Antiferromagnetism in a nanocrystalline high entropy oxide (Co,Cu,Mg,Ni,Zn)O: magnetic constituents and surface anisotropy leading to lattice distortion. Acta Mater. 2020;200:526–36.
39. Mazza AR, Skoropata E, Sharma Y, Lapano J, Heitmann TW, Musico BL, et al. Designing magnetism in high entropy oxides. Adv Sci. 2022;9:2200391.
40. Zhou Y, Dong S, Shan C, Ji K, Zhang J. Two-dimensional ferroelectricity induced by octahedral rotation distortion in perovskite oxides. Phys Rev B. 2022;105:075408.
41. Rost CM, Rak Z, Brenner DW, Maria J-P. Local structure of the $Mg_xNi_xCo_xCu_xZn_xO$ ($x = 0.2$) entropy-stabilized oxide: an EXAFS study. J Am Ceram Soc. 2017;100:2732–38.
42. Jiang B, Pitike KC, Lin D-Y, Purdy SC, Wang X, Zhao Y, et al. Local cation ordering in compositionally complex Ruddlesden–Popper $n = 1$ oxides. APL Mater. 2023;11:051104.
43. McCormack SJ, Navrotsky A. Thermodynamics of high entropy oxides. Acta Mater. 2021;202:1–21.
44. Almishal SSI, Sivak JT, Kotsonis GN, Tan Y, Furst M, Srikanth D, et al. Untangling individual cation roles in rock salt high-entropy oxides. Acta Mater. 2024;279:120289. https://doi.org/10.48550/arXiv.2405.07918
45. Degen T, Sadki M, Bron E, König U, Nénert G. The HighScore suite. Powder Diffr. 2014;29:S13–S18.
46. Kropf AJ et al. The new MRCAT (Sector 10) bending magnet beamline at the advanced photon source. AIP Conf Proc. 2010;1234:299–302.
47. Ravel B, Newville M. ATHENA, ARTEMIS, HEPHAESTUS: data analysis for X-ray absorption spectroscopy using IFEFFIT. J Synchrotron Radiat. 2005;12:537–41.
48. Arcon I, Mirtic B, Kodre A. Determination of valence states of chromium in calcium chromates by using X-ray absorption near-edge structure (XANES) spectroscopy. J Am Ceram Soc. 1998;81:222–24.
49. Chantler CT, Olsen K, Dragoset RA, Chang J, Kishore AR, Kotochigova SA, et al. X-ray form factor, attenuation, and scattering tables. NIST. 2009.
50. Hegde MS. Epitaxial oxide thin films by pulsed laser deposition: retrospect and prospect. J Chem Sci. 2001;113:445–58.
51. Schou J. Physical aspects of the pulsed laser deposition technique: the stoichiometric transfer of material from target to film. Appl Surf Sci. 2009;255:5191–98.
52. Guda AA, Guda SA, Martini A, Kravtsova AN, Algasov A, Bugaev A, et al. Understanding X-ray absorption spectra by means of descriptors and machine learning algorithms. Npj Comput Mater. 2021;7:1–13.
53. Wu TS, Chen YC, Shiu YF, Peng HJ, Chang SL, Lee HY, et al. Correlation between oxygen vacancies and magnetism in Mn-doped Y_2O_3 nanocrystals investigated by defect engineering techniques. Appl Phys Lett. 2012;101:022408.
54. Chou S-C, Tso K-C, Hsieh Y-C, Sun B-Y, Lee J-F, Wu P-W. Facile synthesis of Co_3O_4@CoO@Co gradient core@shell nanoparticles and their applications for oxygen evolution and reduction in alkaline electrolytes. Materials. 2020;13:2703.
55. Bridges F, Booth CH, Anderson M, Kwei GH, Neumeier JJ, Snyder J, et al. Mn K-edge XANES studies of $La_{(1-x)}A_{(x)}MnO_3$ systems, A = Ca, Ba, Pb. Phys Rev B. 2001;63:214405.
56. de Groot F, Vankó G, Glatzel P. The 1s x-ray absorption pre-edge structures in transition metal oxides. J Phys Condens Matter. 2009;21:104207.
57. Almishal SSI, Tan Y, Kotsonis GN, Sivak JT, Alem N, Chen L-Q, et al. Order evolution from a high-entropy matrix: understanding and predicting paths to low temperature equilibrium. arXiv. 2024:15708. https://doi.org/10.48550/arXiv.2404.15708
58. Kotsonis GN, Almishal SSI, Miao L, Caucci MK, Bejger GR, Ayyagari SVG, et al. Fluorite-structured high-entropy oxide sputtered thin films from bixbyite target. Appl Phys Lett. 2024;124:171901.
59. Zhang J, Yan J, Calder S, Zheng Q, Mcguire MA, Abernathy DL, et al. Long-range antiferromagnetic order in a rocksalt high entropy oxide. Chem Mater. 2019;31:3705–11.

SUPPORTING INFORMATION

Additional supporting information can be found online in the Supporting Information section at the end of this article.

How to cite this article: Niculescu GE, Bejger GR, Barber JP, Wright JT, Almishal SSI, Webb M, et al. Local structure maturation in high entropy oxide $(Mg,Co,Ni,Cu,Zn)_{1-x}(Cr,Mn)_xO$ thin films. J Am Ceram Soc. 2025;108:e20171. https://doi.org/10.1111/jace.20171